Crustal thickness variations in the Zagros continental collision zone (Iran) from joint inversion of receiver functions and surface wave dispersion

M. Tatar & A. Nasrabadi

Journal of Seismology

ISSN 1383-4649

J Seismol
DOI 10.1007/s10950-013-9394-z

J Seismol
DOI 10.1007/s10950-013-9394-z

ORIGINAL ARTICLE

Crustal thickness variations in the Zagros continental collision zone (Iran) from joint inversion of receiver functions and surface wave dispersion

M. Tatar · A. Nasrabadi

Received: 24 December 2012 / Accepted: 26 August 2013

Abstract Variations in crustal thickness in the Zagros determined by joint inversion of P wave receiver functions (RFs) and Rayleigh wave group and phase velocity dispersion. The time domain iterative deconvolution procedure was employed to compute RFs from teleseismic recordings at seven broadband stations of INSN network. Rayleigh wave phase velocity dispersion curves were estimated employing two-station method. Fundamental mode Rayleigh wave group velocities for each station is taken from a regional scale surface wave tomographic imaging. The main variations in crustal thickness that we observe are between stations located in the Zagros fold and thrust belt with those located in the Sanandaj–Sirjan zone (SSZ) and Urumieh–Dokhtar magmatic assemblage (UDMA). Our results indicate that the average crustal thickness beneath the Zagros Mountain Range varies from ~46 km in Western and Central Zagros beneath SHGR and GHIR up to ~50 km beneath BNDS located in easternmost of the Zagros. Toward NE, we observe an increase in Moho depth where it reaches ~58 km beneath SNGE located in the SSZ. Average crustal thickness also varies beneath the UDMA from ~50 km in western parts below ASAO to ~58 in central parts below NASN. The observed variation along the SSZ and UDMA may be associated to ongoing slab steepening or break off in the NW Zagros, comparing under thrusting of the Arabian plate beneath Central Zagros. The results show that in Central Iran, the crustal thickness decrease again to ~47 km below KRBR. There is not a significant crustal thickness difference along the Zagros fold and thrust belt. We found the same crystalline crust of ~34 km thick beneath the different parts of the Zagros fold and thrust belt. The similarity of crustal structure suggests that the crust of the Zagros fold and thrust belt was uniform before subsidence and deposition of the sediments. Our results confirm that the shortening of the western and eastern parts of the Zagros basement is small and has only started recently.

Keywords Crustal structure · Iran · Zagros · Receiver functions · Surface wave dispersion · Joint inversion · Continental collision

M. Tatar (✉) · A. Nasrabadi
International Institute of Earthquake Engineering and Seismology,
Tehran, Iran
e-mail: mtatar@iiees.ac.ir

A. Nasrabadi
Kerman University of Technology for Graduate studies,
Kerman, Iran

1 Introduction

The Zagros fold and thrust belt with two other NW-trending parallel tectonometamorphic and magmatic belts of Sanandaj–Sirjan zone (SSZ) and the Urumieh–Dokhtar magmatic assemblage (UDMA; Fig. 1)) were formed as result of the Arabia–Eurasia convergence during the Mesozoic and Cenozoic period (Berberian and King 1981; Berberian et al. 1982; Mouthereau et al. 2012)

The Zagros Mountain belt is approximately 1,500 km long and 200 to 400 km wide, which runs from Eastern Turkey, where it joins with the high topography of the

Published online: 13 September 2013

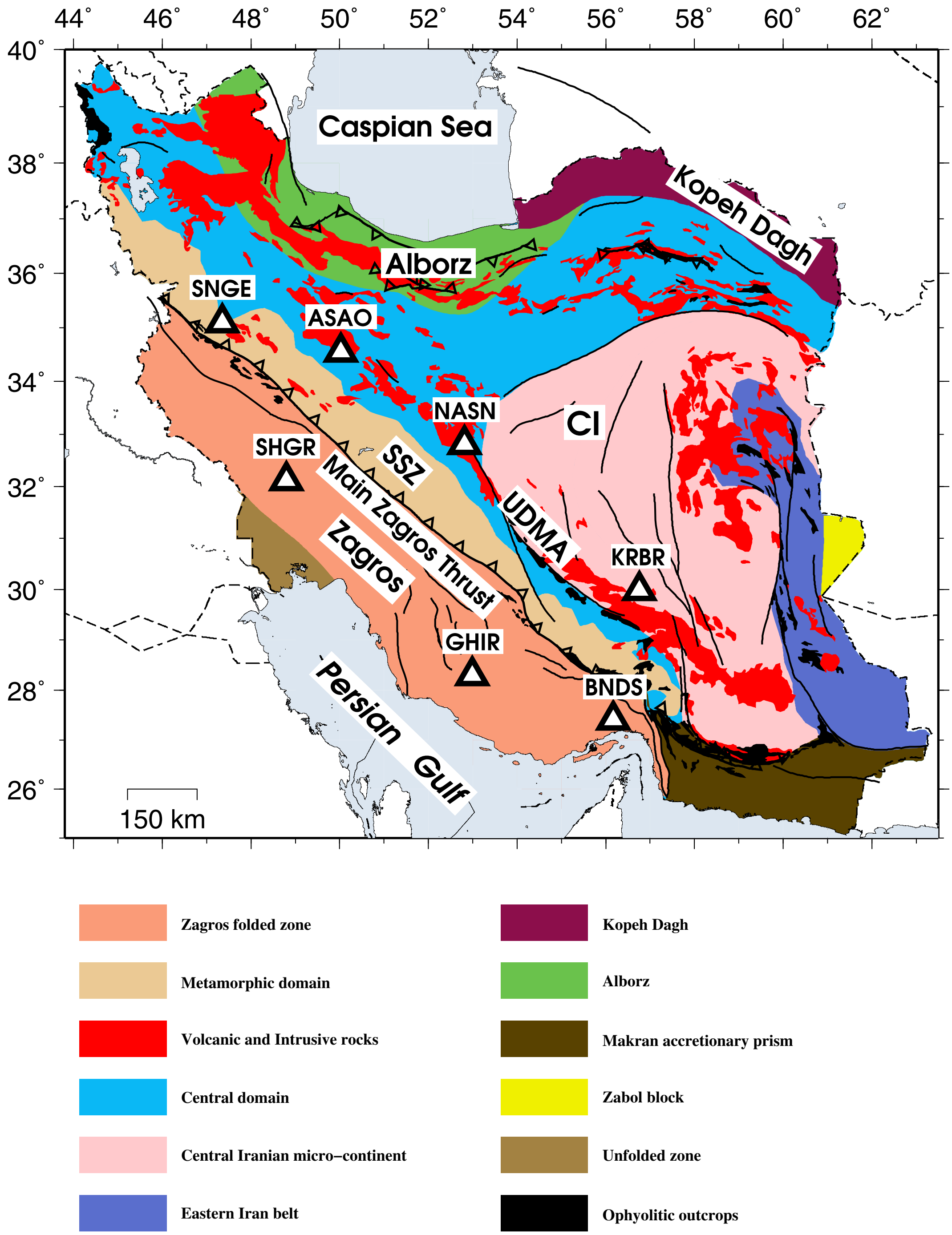

Fig. 1 Location map of the seismological stations of Iranian National Seismic Network (*INSN*) including different seismotectonic zones of Iran. Stations used in this study are plotted as *black–white triangles*. The main faults are shown as *thick black lines*. Geological map modified from the structural map of NGDIR (National Geoscience Database of Iran, http://www.ngdir.ir)

Anatolian Plateau and Lesser Caucasus, to the Oman Sea, where it connects to the Makran subduction zone. The Zagros deformation is characterized by constant wavelength folding, thrusting, and strike slip faulting (Hatzfeld et al. 2010). The Zagros fold and thrust belt resulted from the collision of the Arabian Plate with the continental crust of Central Iran. Zagros is considered as an example of a young continent–continent collision belt (Bird et al. 1975; Bird 1978; Hatzfeld et al. 2003). The suggested age of the initial collision along the Zagros suture varies from Late Cretaceous to Pliocene (Berberian and King 1981; Allen et al. 2004). Convergence between Arabia and Eurasia has been continuous since Late Cretaceous times, with a late episode of accentuated shortening during the Pliocene–Quaternary (Hatzfeld et al. 2010). The belt lies on the former Arabia passive margin that is covered by up to 10 km of Infracambrian to Miocene sediments (e.g., Stöcklin 1974; Stoneley 1981). Zagros accommodates about 6–7.5 mm/year of NNE–SSW shortening, which correspond to ~30 % of total convergence between Arabia and Eurasia (Vernant et al. 2004; Walpersdorf et al. 2006; Hatzfeld et al. 2010).

Although Zagros is considered as one of the most seismically active intercontinental fold and thrust belts in the word, but no instrumental earthquake with magnitude (Mw) greater than 6.7 and no coseismic ruptures have been observed in this highly deformed belt, except for one earthquake in 1990 (Mw=6.4) located at the eastern termination of the high Zagros fault (Walker et al. 2005). Seismicity in the Zagros Mountains is shallow, with focal depths ranging not more than 20 km restricted mainly to the region between the main Zagros thrust (MZT) and the Persian Gulf. Most of the larger earthquakes occur on high-angle reverse planes striking parallel to the trend of the fold axes (Jackson 1980; Jackson and McKenzie 1984; Ni and Barazangi 1986; Maggi et al. 2000; Tatar et al. 2004; Hatzfeld et al. 2010; Engdahl et al. 2006).

The SSZ (Fig. 1), located to the north of the MZT, consist of sedimentary and metamorphic Paleozoic to Cretaceous rocks formed in the former active margin of an Iranian microcontinent drifted during the Late Jurassic (Berberian and Berberian 1981; Golonka 2004; Mouthereau et al. 2012). It has undergone various metamorphic episodes during the subduction of the Tethyan Ocean under the Iranian block, the obduction of ophiolites along the MZT, and the final continental collision (Stocklin 1968; Davoudzadeh et al. 1997). The SSZ is considered as the metamorphic core of the Zagros accretionary complex built by the thickening of distal crustal domains of the Arabian margin (Alavi 2004; Moghadam et al. 2010; Mouthereau et al. 2012). The metamorphic rocks are unconformably overlain by the Lower Cretaceous Orbitolina limestone of the Central Iranian domain (Stöcklin 1974). The SSZ overthrusted the Zagros sedimentary sequence along the MZT (Stocklin 1968; Agard et al. 2005).

The UDMA (Fig. 1) is an Andean-style volcanic arc striking parallel to the Zagros Mountains and located between the SSZ and Central Iran. UDMA is composed of a variety of intrusive igneous rock types, and a range of extrusive material (Alavi 1994), varying in age from the late Jurassic to Quaternary (Molinaro et al. 2005). The volcanics of this assemblage supposed to be in association with the continuing subduction of the Neo-Tethyan slab (Alavi 1994). This assemblage has not been volcanically active since the Quaternary, although it is believed that the peak activity to be during the Eocene (Alavi 1994).

Recent tomography constraints (Agard et al. 2011; Vergés et al. 2011; Chang et al. 2010) reveal a discontinuous Neo-Tethyan slab, dipping about 50° to the NE beneath the NW Zagros, in contrast of the cold Arabian lithosphere beneath Central Iran (Chang et al. 2010; Paul et al. 2010; Simmons et al. 2011), which is characterized as a low dip angle underthrusting/subducting slab (Mouthereau et al. 2012). It is believed that the observed variation along the SSZ and UDMA may be associated to the ongoing slab steepening or break off in the NW Zagros, comparing under thrusting of the Arabian plate beneath Central Zagros (Mouthereau et al. 2012).

Crustal structure studies published prior to 1990 mainly dealt with gravity data. Dehghani and Makris (1984) computed a crustal thickness map from the gravity variations of Iran. According to their results, the observed negative gravity anomaly gives a maximum crustal thickness of 50–55 km located beneath the MZT, and a normal thickness of 40 km beneath the Persian Gulf coast and Central Iran (Paul et al. 2010). However, the more detailed Bouguer anomaly modeling of Snyder and Barazangi (1986) indicates a maximum crustal thickness of 55–60 km beneath the MZT.

Studies using receiver functions for Zagros show variability in crustal thickness. Most of them indicate an average crustal thickness of 45 km beneath the Zagros fold and thrust belt (Hatzfeld et al. 2003; Paul et al. 2006, 2010; Afsari et al. 2011), increasing near the MZT, and reaches 67 km beneath the Sanandaj–Sirjan metamorphic zone (Paul et al. 2006, 2010; Yamini-Fard et al. 2006). Hatzfeld et al. (2003) and Paul et al. (2006, 2010) measured a crustal thickness of ~46 km beneath the Central Zagros using receiver functions. Elsewhere, again using the same technique, Afsari et al. (2011) found an average

Moho depth of about 42 km beneath the Northwest Zagros. Farther northeast, Paul et al. (2006) inferred crustal thickness of 61–65 km beneath the Sanandaj–Sirjan metamorphic zone. They proposed that this localized thickening results from the overthrusting of the crust of Central Iran onto the Zagros crust along the MZT.

We know that the relative character of the receiver function constraints makes the inversion problem implicitly non-unique (Ammon et al. 1990). The Vp/Vs ratio is a critical parameter in the time to depth migration of receiver functions. As discussed by Paul et al. (2006) in all abovementioned studies, the uncertainty on absolute depths is large (up to 5 km), as we have no precise estimate of the crustal Vp and Vp/Vs models. We hope, in this research, to overcome this limitation by incorporating the constraints on the absolute velocities from the dispersion estimates (Ozalaybey et al. 1997; Julia et al. 2000) by jointly inversion of the receiver function and surface wave dispersion data. Therefore, the aim of this paper is to investigate on the variation of the crustal thickness beneath the different parts of the Zagros from the Zagros fold and thrust belt (beneath SHGR, GHIR, and BNDS stations), to the Sanandaj–Sirjan (beneath SNGE station), and to the UDMA (beneath ASAO and NASN) and the western part of Central Iranian microcontinent (beneath KRBR) from joint inversion of two independent datasets, receiver functions, and fundamental mode Rayleigh wave group and phase velocity dispersion.

2 Data and methodology

Receiver functions were computed from ~220 teleseismic events, located at epicentral distances of 30–90°, recorded by seven seismic stations of broadband Iranian National Seismic Network (INSN) from May 16, 2004 to July 29, 2005. For one of the stations, GHIR, we used more than 4 years of teleseismic waveforms. These stations are located in different seismotectonic zones of Iran (Fig. 1). Rayleigh wave phase velocity dispersion curves were estimated employing two-station method on more than 3 years data recorded by 23 broadband stations of INSN. Information about the group velocity dispersion comes from tomographic images between 15 and 70 s period produced by a study of regional fundamental mode Rayleigh waves propagating across Iran and surrounding regions (Rham 2009).

2.1 Receiver function estimates

The teleseismic receiver function is an efficient seismic tool for imaging underground geology. Receiver functions represent the local earth response to the arrival of nearly vertical P waves beneath a three-component broadband seismometer (Langston 1979), and mathematically, they are the transfer functions between the P wave with all associated P multiples and reverberations, and the Ps phases with their multiples and reverberations (Ammon 1991). More than 1 year of teleseismic waveforms were selected in order to obtain receiver function estimates beneath seven stations of INSN network. The data were analyzed in the manner described by Abbassi et al. (2010). We computed the receiver functions using the methodology of Ligorria and Ammon (1999) which has higher stability with noisy data compared to frequency-domain methods and obtained true amplitude radial and tangential receiver functions. The instrument response and the gains were corrected before proceeding to the receiver function deconvolution. High frequencies are excluded by using a Gaussian filter. We set the parameter a of the Gaussian filter to 1.00, 1.6, and 2.5 which gives an effective high-frequency limit of about 0.5, 0.8, and 1.2 Hz in the P wave data, respectively. All receiver functions were grouped by azimuth (<10°) and distance (<10°), and in order to improve the signal-to-noise ratio, the individual receiver functions within each group were stacked. Figure 2 shows the resultant radial receiver functions for Gaussian parameter of 1 and 1.6 at GHIR station. Using an average crustal Vs=3.7 km s^{-1}, this gives a minimum resolvable wavelength of $\lambda=\pm7.4$ km. Considering the minimum resolvable length scale in such an inversion equal to $\lambda/4$, only features greater than 1.85 km are resolvable in the final model.

2.2 Surface wave dispersion observations

Surface waves velocity dispersion primarily depends on S wave velocity, with some dependence on P wave velocity, and little dependence on density (Ozalaybey, et al. 1997). In previous studies, it has been shown that it improves the inversions of receiver functions for crustal structure (Julia et al. 2000). Surface waves velocity dispersion provide information on the absolute seismic shear velocity, but are relatively insensitive to sharp velocity changes. The group velocities were incorporated into our joint inversion scheme from an independent surface wave tomography study by

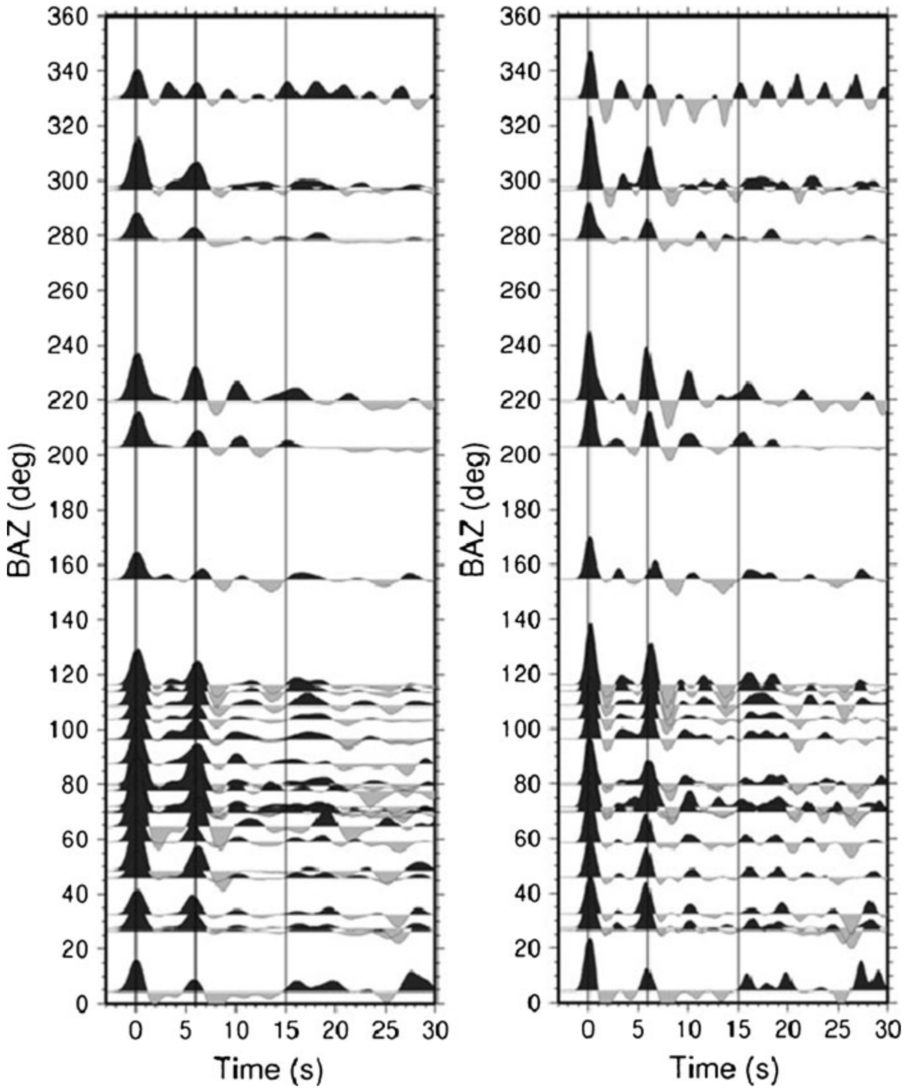

Fig. 2 Stacked radial receiver functions for GHIR station listed for each of the two Gaussian filter parameter 1.0 (*left*) and 1.6 (*right*). All events are generated using iterative deconvolution

Rham (2009). Group velocities from regional events recorded at permanent and broadband stations were measured for fundamental mode Rayleigh waves within the 10–70-s period range. The region was parameterized using a uniform, 1×1°, grid of constant slowness cells. The dispersion curve is the result of tomographic imaging for each period separately. Fundamental mode Rayleigh wave group velocities are taken from the corresponding tomographic cell containing the stations.

Rayleigh wave phase velocity dispersion curves were estimated by employing two-station method of Aki and Richard (2002). More than 3 years of teleseismic waveforms, nearly aligned along the same great circle path (<10°) as station pairs, recorded by seven broadband stations of INSN network (GHIR, BNDS, SHGR, SNGE, NASN, ASAO, and KRBR), were used to establish the Rayleigh wave phase velocity dispersion curve between the possible station pairs. From April 15, 2004 to April 16, 2007, all teleseismic earthquakes with epicentral distances of 30–90° and magnitudes greater than 5, 90–130° and magnitudes greater than 6, and 130–170° and magnitudes greater than 6.5 were selected for establishing an appropriate database of events for surface wave phase velocity estimation. First, the instrument response was removed from all vertical component seismograms. They were then decimated to a sampling rate of 1 Hz. The two horizontal components (N-S, E-W) were rotated to produce radial and tangential components, but only Rayleigh waves were inspected for all considered events. The desired part of the waveform is isolated from the seismogram using frequency–time domain analysis (FTAN) (Levshin et al. 1992). The technique filters the data with a set of narrow band Gaussian filters, with the important difference to conventional multiple filter techniques that the instantaneous phase (rather than the central frequency of the narrowband filters) is used to determine the frequency of group arrival picks. This method has some advantages because it corrects for the fall-off of the event amplitude spectrum at low frequencies (Shapiro and Singh 1999) and that measurements are less biased by spectral holes (Rapine et al. 2003). The peaks of the envelopes of the filtered traces then define the group arrival times at the different frequencies. Figure 3a shows an example of vertical seismogram for the event in April 13, 2007 with epicenter distance of 128° recorded by GHIR station, and Fig. 3b shows the FTAN diagram of the seismogram.

The fundamental mode Rayleigh wave is selected constructing energy versus period diagram of the surface wave. This curve is used to construct a phase-matched filter (Herrin and Goforth 1977), whereby the desired fundamental mode surface wave signal can be extracted from the observed waveform. The filter identifies and removes multipathing arrivals to improve the quality of the determined dispersion curves. In this step, the phase at a station i, φi, is measured as the instantaneous phase at the group arrival times tigroup(ω) as determined by frequency–time analysis of Levshin et al. (1992). The phase values are then corrected for the fact that measurements are taken at different times, and unwrapped (Rapine et al. 2003),

$$\varphi_i'(\omega) = \varphi_i(\omega) - \omega t_i^{\,group}(\omega) + 2\pi N$$

The term 2πN is added to compensate for the number of complete cycles separating the two phases. Phase velocity dispersion data is obtained for each pair stations using Wiener (1949) filter. Wiener filter transforms phase differences φ to time delays using dT=(φ/2πf). For smoothing, the spectra Hanning window is applied to the cross-correlation of the two signals. Then, phases with a coherence of less than 0.95 were rejected. In next step, we inverted the time delay for each event to obtain the best slowness vector (P) and stored distances (D) between station pairs projected on to the slowness vector as well as the misfit (F). The misfit is the mean absolute difference between the observed and estimated delays. Finally, the phase velocity is calculated at each frequency using all observed distance and delay time points that are associated with a misfit lower than a certain threshold. The velocity is calculated as the inverse of the slope and the best-fitting line Δt=D/V (Pedersen et al. 2003). The procedure is repeated for all frequencies and corresponds to averaging the phase velocities associated with each event and weighted by the number of station couples used for the event, as described by Pederson et al. (2003). To minimize uncertainty, which is due from identifying the main dispersion ridge separating the "direct arrival" from the surface wave coda at periods below 25 s, and truncating the measurements appropriately at long periods as the signals weaken, we compute an average dispersion curve from several events with a correlation coefficient of 0.95 or higher for each station pair, instead of measuring the phase velocities from a single event. Knowing the Rayleigh waves show almost the same scatter at short periods (Tezel et al. 2007), we exclude the short period dispersion date (<15 s). Figure 4 shows the phase velocity dispersion curve for path SNGE–ASAO.

Surface wave periods less than 100 s were sufficient to sample crust and uppermost mantle depths needed in the current study. Therefore, surface waves with periods greater than 100 s were discarded. We computed the fundamental-mode Rayleigh wave phase velocity dispersion curves for interstation pairs as follows: GHIR–SHGR, GHIR–BNDS, SHGR–BNDS, SNGE–ASAO, ASAO–NASN, ASAO–KRBR, and NASN–KRBR.

2.3 Joint inversion

Both the Rayleigh wave and receiver function energy are found in the P–Sv plane and are, therefore, sensitive to Vsv in the crust, whereas the Love wave is restricted to the SH plane. This means that both datasets are sampling the same crustal parameter. However, receiver functions constrain velocity contrasts and relative vertical travel times beneath the recording station, while dispersion velocities constrain average absolute S wave velocity values within frequency-dependent depth ranges. The relative character of the receiver function constraints makes the inversion problem implicitly non-unique (Ammon et al. 1990), but this limitation can be overcome by incorporating the constraints on the

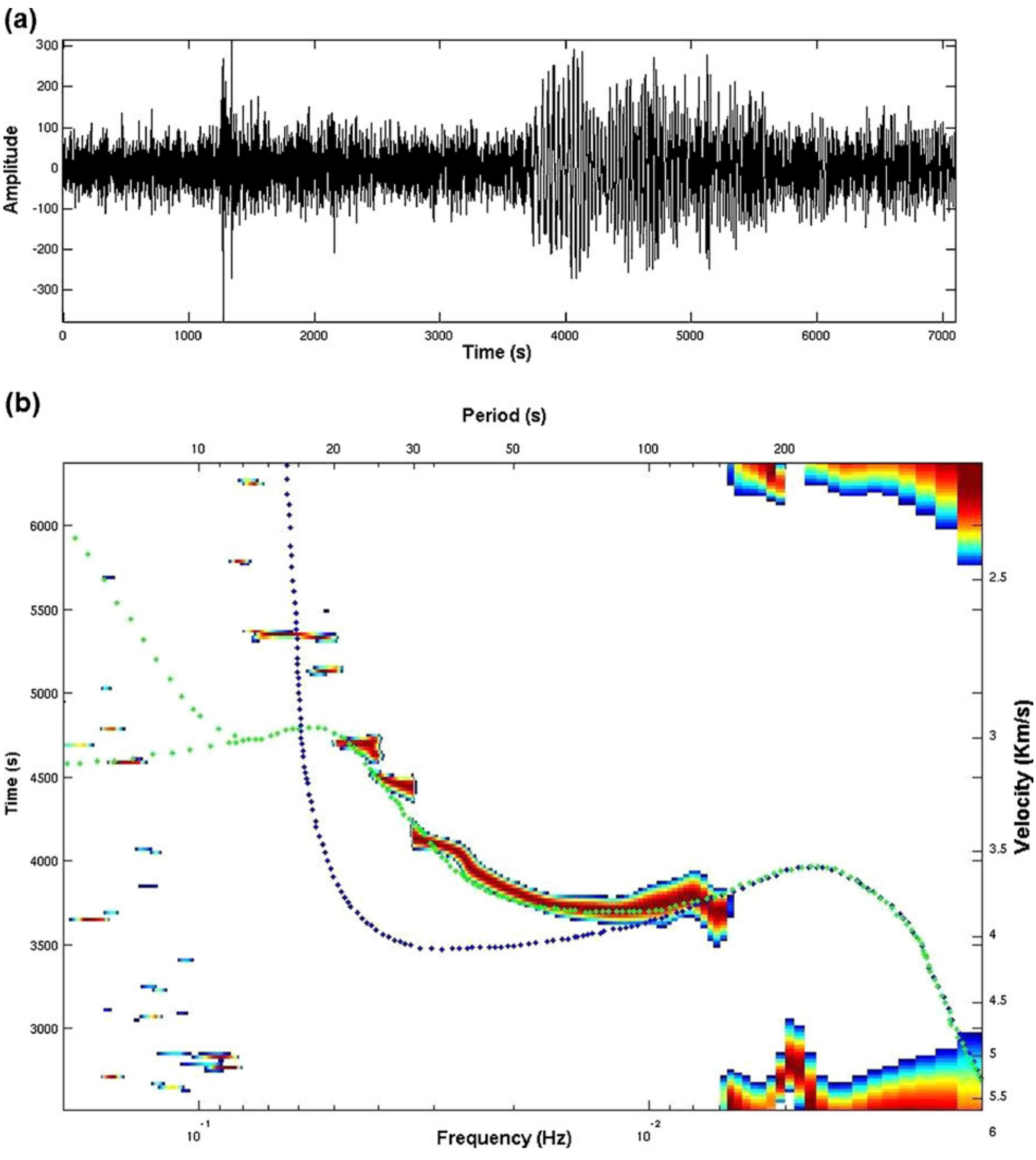

Fig. 3 **a** Vertical seismogram for event 2007/04/13 with epicenter distance of 128° recorded by GHIR station. **b** The desired part of the seismogram is isolated from the seismogram using frequency–time domain analysis (FTAN) (Levshin et al. 1992). The peaks of the envelope of the filtered trace define the group arrival times at the different frequencies

absolute velocities from the dispersion estimates (Julia et al. 2000). The datasets are, thus, complementary. The simultaneous inversion of two datasets to find a single velocity model was carried out using the computer program in seismology package of Hermann and Ammon (2003). This finds a single velocity structure that minimizes the following objective function:

$$S = \frac{(1-P)}{N_r}\sum_{i=0}^{Nr}\left(\frac{O_{ri}-P_{ri}}{\sigma_{ri}}\right)^2 + \frac{P}{N_s}\sum_{j=0}^{Ns}\left(\frac{O_{sj}-P_{sj}}{\sigma_{sj}}\right)^2 \quad (1)$$

Fig. 4 Fundamental mode Rayleigh wave average phase velocity dispersion curve for path SNGE-ASAO

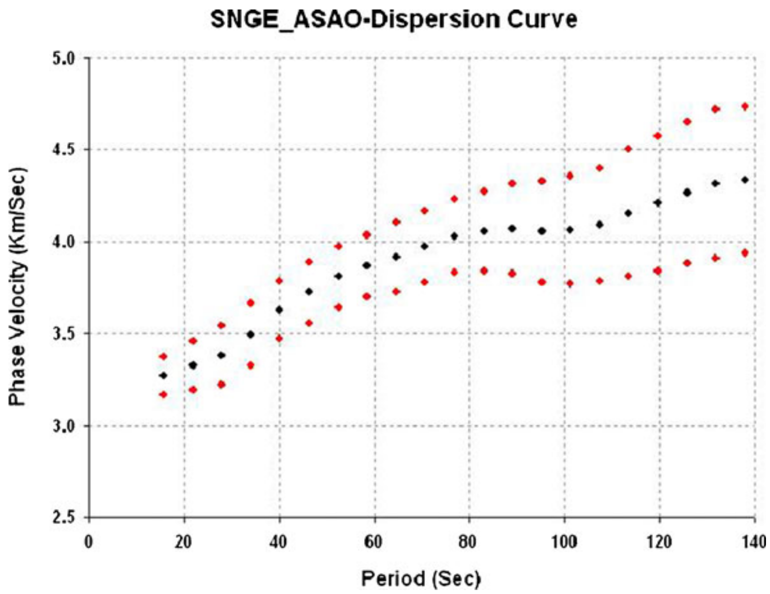

Where O_{ri} is observed receiver function at time t_i, P_{ri} is predicted receiver function at time t_i, σ_{ri} is standard error of observation at t_i, O_{sj} is jth observed surface wave dispersion, P_{sj} is jth predicted surface wave dispersion point, σ_{sj} is standard error of jth surface wave observation, N_r is total number of receiver function point, N_s is total number of surface wave dispersion points, p is influence factor, $0 \le P \le$, p=0 forces receiver function solution, and p=1 forces surface wave solution.

The inversion package requires that the real velocity structure be represented by a set of flat-lying, homogeneous, isotropic velocity layers. During inversion, the vertical extent of each layer remains fixed, whereas the velocity is free to change (within user-defined damping limits). The starting model comprised layers that were 1-km thick for the top 6 km of the model space, 2-km thick between 6 and 66 km, and 4-km thick between 66 and 78 km. The starting velocity for each layer in the model was Vp=8.0 km/s, which equates to upper mantle velocities.

3 Results

We performed joint inversion for all back azimuths of all stations, but we present the procedure in detail for station GHIR, which is located in the Central Zagros (52.99°E, 28.28°N) (Fig. 1). Among 280 good quality computed receiver functions with very sharp Ps phases, 24 stacks were made for different back azimuths (Fig. 2), and a total of 14 were modeled for crustal structure beneath the GHIR station.

Figure 5 summarizes results of joint inversion for the receiver structure at GHIR based on the receiver function stack with a mean back azimuth of 47° with Rayleigh wave group velocity dispersion curve. This stack contains eight events which range in epicenter distance from 41–50°. Radial receiver function and the surface wave group velocity dispersion curve are shown at the upper and lower right panels, respectively. The left panel shows the initial and estimated velocity model. The blue dashed line denotes the initial model, the red solid line the predictions for the model, and the solid black line denotes the final crustal model consisting of the minimum number of crustal layers required to simultaneously fit the receiver function and surface wave data. From this figure, we infer that the Ps delay time is nearly 6 s. The fit to both observed and predicted receiver functions and observed and predicted group velocities dispersion values are good.

We ran joint inversion with p=0.1–0.9 range to find the best match of observed and predicted receiver function/surface wave. The p=0.2 solution provides the best waveform fit to utilize in the 2-D solution. The shear velocity–depth profile of the p=0.2 solution exhibits complex features, as can be summarized as follows. The software does not allow the use of standard errors for the receiver functions (equivalent to the ±1 σ calculated in the stacking process), instead the standard error of the fit of the model to the stacked receiver function is

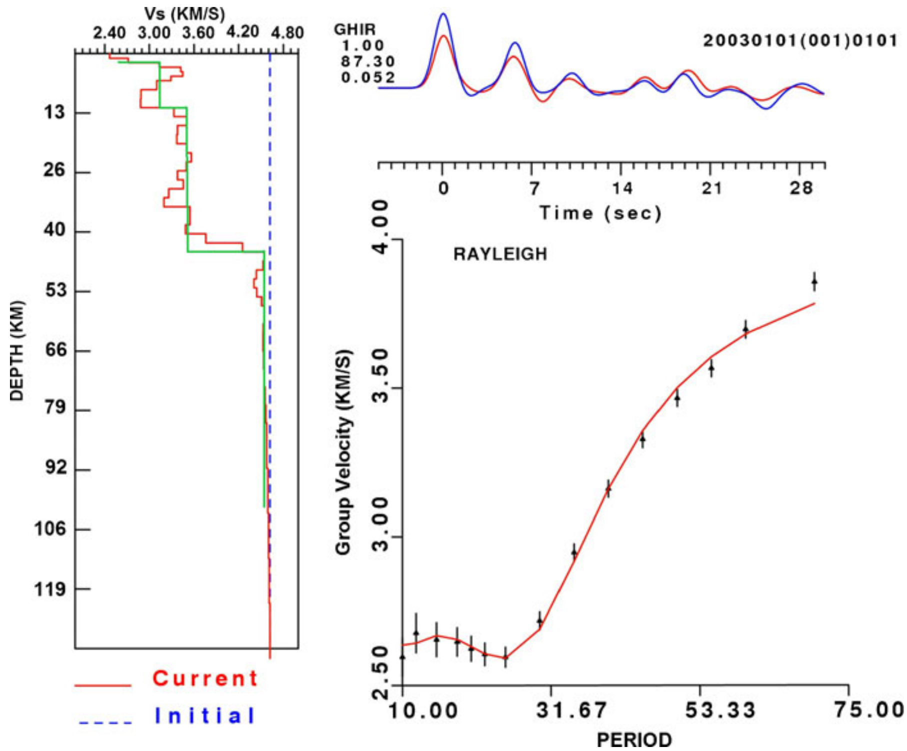

Fig. 5 Joint inversion results for station GHIR for 41–50° back azimuth bin receiver function stack. The receiver function is at the *upper right*, the surface wave group velocity dispersion at the *lower right*, and the model at the *left*. The *blue dashed line* denotes the initial model, the *red solid line* the predictions for the model, and the *solid green line* denotes the final crustal model consisting of the minimum number of crustal layers required to simultaneously fit the receiver function and surface wave data

used. For the surface wave dispersion, the correct measured error limits are used.

For station GHIR, all the models contain a rapid velocity increase during the few first kilometers below the surface, a lower crust with a rather constant velocity, and a gradational crust to mantle transition. There is a thin (~2 km) of low-velocity material (Vs<2.7 km s^{-1}) at the surface and a 10-km thick sediments layer (Vs=3.0–3.2 km s^{-1}), above a ~34-km thick crystalline crust (Vs=3.5–3.7 km s^{-1}). Moho is located at ~46-km depth; however, the Moho interface comprises a series of small velocity steps (Fig. 5). We interpret the Moho as the depth at which the shear wave velocity reaches sustained values typical of the sub-Moho mantle (Vs=4.5 km s^{-1}).

It is important to establish how much of the complexity seen in the model (Fig. 5) results from the fitting of noise in the receiver function and surface wave data. In order to eliminate unnecessary complexity, we simplified the model resulted from the previous step by amalgamating the 2-km thick layer with the same velocity as thicker layer. However, we took care so that the simplest resulting model fitted the observed data. The method and approach we used are described in detail in Abbassi et al. (2010). As shown in Fig. 6, we took the output model of the joint inversion (Fig. 5) and fit the simplest four-layered model to it. Synthetic dispersion curves and receiver functions are produced for this layered half space, and compared to both the original data, and those produced by the joint inversion. As an error analysis, the resolution of the final simple crustal model was tested by offsetting the Moho by ±5, ±2, and ±1 km from the model-determined Moho depth. Synthetics were then produced for this new model and compared to the final model results, the joint inversion, and the original data. This approach showed that the Moho could be offset up to ±2 km before the synthetics had varied away from the data by such a degree as to be visually different. In this way, we estimated errors of 2.0 km on the calculated Moho depth for each stacked receiver function.

We followed the same procedure described earlier for selecting and stacking the receive functions computed using a Gaussian parameter (α) of 1.6. As expected, the

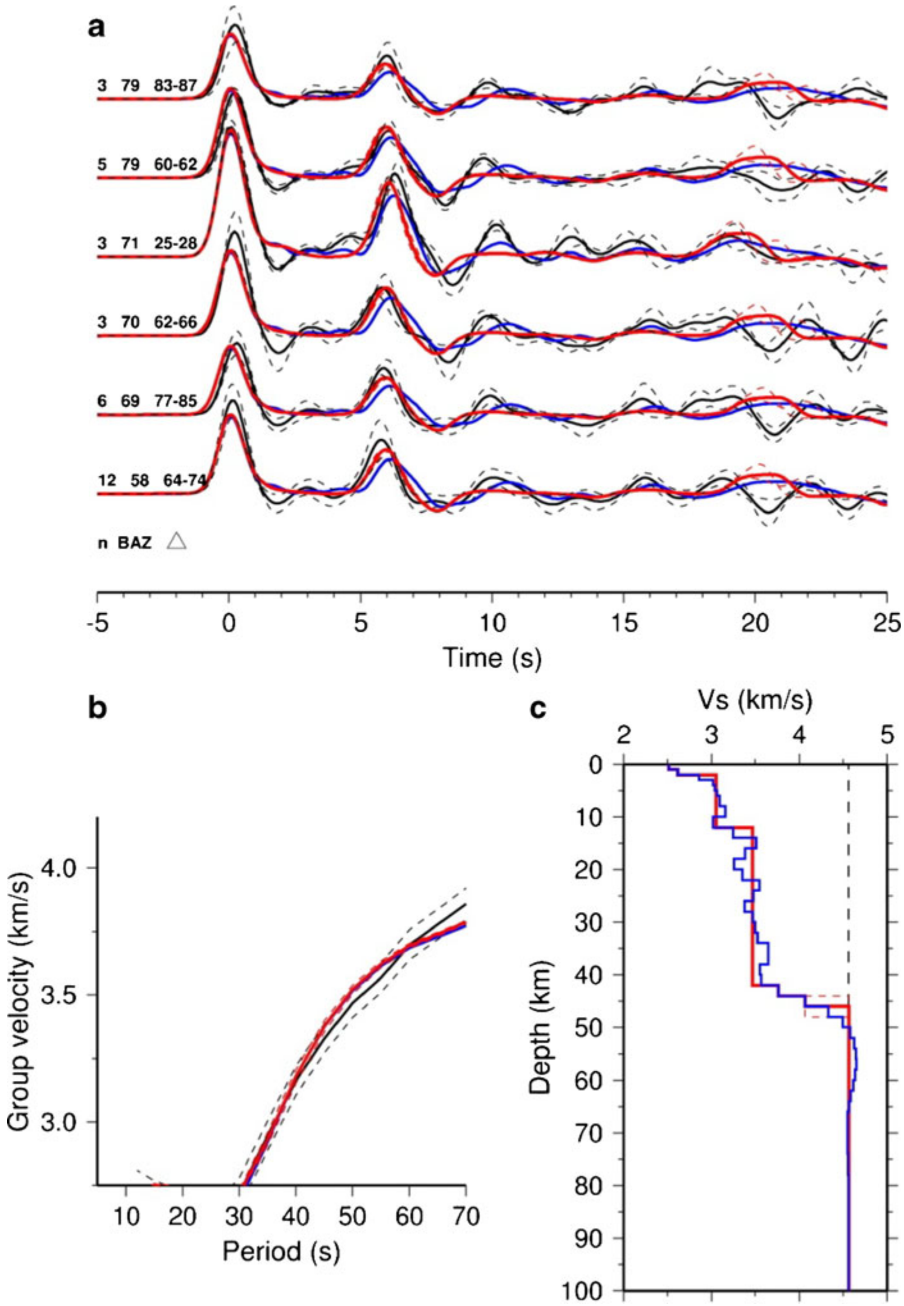

Fig. 6 Forward modeling results for the six receiver function stacks computed with Gaussian parameter of 1.6. The original receiver function and dispersion curve (*solid black lines*) and their associated standard deviations (*black dashed*) are shown, along with the receiver function and dispersion curve for the joint inversion model (*blue*) and the simplified forward model, synthetic receiver function, and synthetic dispersion curve for the forward modeling (*red*). The initial model used for the joint inversion is shown in *black dashed line*. The different back azimuth stacks are at the *top*, the surface wave dispersion at the *bottom-left*, and the model at the *right*. As we observe, both the initial multilayer (from Joint Inversion) and the simplified model provide a reasonable fit to the observed receiver function and dispersion curve

stacked receiver functions contain high frequencies, which impose more complexity in the resulted crustal structure. However, we tried jointly inverting them with Rayleigh wave and group velocity dispersion data. We tried to show that the goodness of fit is still high for new computed receiver functions. Although the Ps conversions at the Moho depth are different, Fig. 6 indicates very similar results as were obtained for the previous dataset (α=1.0). In most of the models, the crust to mantle transition zone is composed of a series of small velocity steps located at 46±2 km depth.

The results for six acceptable receiver function stacks with Gaussian parameter of 1.6 are summarized in Fig. 6. For each stacked receiver function, we used the output model of the joint inversion (Fig. 5) as a starting model, and tried to fit the simplest four- or five-layered model to it. The fit between observed and synthetic dispersion curve and receiver functions is very good.

As can be observed in Fig. 6, the final models contain a thin (~2 km) layer of low-velocity material (Vs<2.8 km/s) below the surface, overlaying a rapid velocity increase of 3.0 km/s. We observe interfaces with sharp velocity increases at ~12 km, a lower crust with a rather constant velocity, and a gradational crust to mantle transition. The Moho discontinuity is composed of a series of small velocity steps located at 46 ±2 km depth. In the simplified model, the crust to mantle transition zone is imaged as a velocity increase of ~0.5–0.7 km/s over a 4 km depth interval.

We also obtained crustal structure beneath GHIR station from joint inversion of receiver function and fundamental mode Rayleigh wave phase velocity dispersion curve (Fig. 7). We used Rayleigh wave average phase velocity dispersion curve for path GHIR–BNDS which crosses almost the same structures within the Zagros. Both GHIR and BNDS stations are located in the Zagros fold and thrust belt, and the path between them are parallel to the main trend of the belt. So, complex lateral heterogeneity perpendicular to the Zagros trend has less effect on the selected phase velocity dispersions curve.

Figure 7 shows the results of joint inversion for the receiver function stack with a mean back azimuth of 47° and GHIR–BNDS phase velocity dispersion curve. Because of high uncertainly in short periods of the

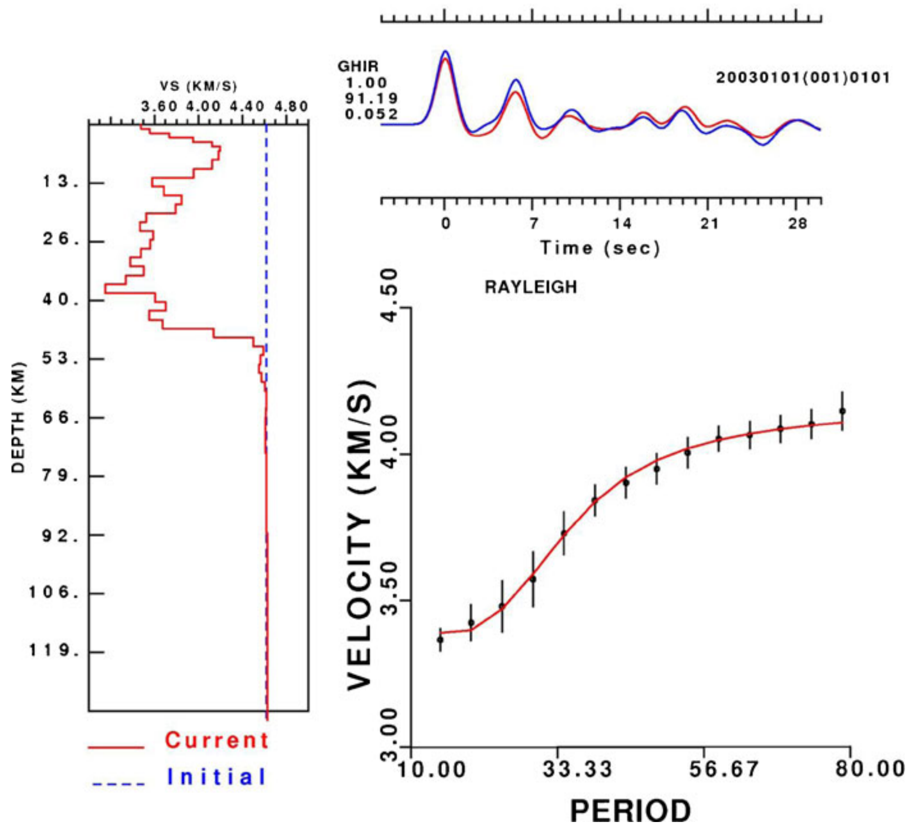

Fig. 7 Results of joint inversion of receiver function and surface wave phase velocity dispersion for station GHIR for 41–50° back azimuth bin receiver function stack. The format of the figure is the same as that in Fig. 5

Table 1 Locations of broadband stations and resulting average values for Moho depth

Station	Lat. N	Long. E	Elevation (m)	Average Moho Depth (km)
Shooshtar (SHGR)	32.108	48.801	150	46
Ghir-Karzin (GHIR)	28.285	52.986	1,200	46
Bandar-Abbas (BNDS)	27.387	56.174	1,500	50
Sanandaj (SNGE)	35.092	47.346	1,940	58
Ashtian-Arak (ASAO)	34.549	50.024	2,217	50
Naein (NASN)	32.799	52.808	2,379	58
Kerman (KRBR)	29.98	56.7610	2,576	47

dispersion curve, it is impossible to recognize the sediments thickness or upper crust sediments interface in the models. But all the models shows sharp Moho interface. Therefore, as the models obtained from joint inversion of receiver function and phase velocity dispersion curve for GHIR station, Moho is located in 48-km depth. Little observed difference in results of two inversions reveals the uniqueness of the result and high-accuracy estimation of the crustal structure and Moho depth beneath the GHIR station.

Following the same procedure described above, we performed the joint inversion of the receiver function and Rayleigh wave group and phase velocity dispersion measurement for seven selected stations of INSN located in the Zagros and adjacent seismotectonic zones. For each station, the stacked receiver functions grouped based on their back azimuth and epicentral distances were inverted jointly using fundamental mode Rayleigh wave group velocities taken from the corresponding tomographic cell containing the stations and appropriate Rayleigh wave phase velocities computed for the closest path to the station, which crosses the same structural units. The results of joint inversion for seven INSN stations are summarized in Table 1 and are shown in Figs. 8 and 9.

Our results indicate that the sedimentary layer and the crystalline crust below SHGR, located in western part of the Zagros, have an average thickness of ~10 and ~34 km, respectively. Beneath GHIR located southwest of the Zagros, as mentioned above, the sedimentary layer and crystalline crust have ~12 and ~34 km thickness, respectively, identical with western part of the Zagros below SHGR. Below BNDS, which is located in easternmost of the Zagros, sedimentary cover is ~14-km thick, while the crystalline crust has an average thickness of ~36 km. The average velocities of the crystalline crust (~3.6 km s^{-1}) are consistent between these three stations, sampling a broad area of the Zagros fold and thrust belt.

Below ASAO and NASN which are located in the UDMA, the sedimentary layer has a thickness of ~5 km and crystalline crust varies from ~44 km beneath ASAO to ~53 km beneath NASN. The average shear wave velocity of crystalline crust beneath these stations is ~3.8 km s^{-1}, which is higher than what we observed for the Zagros fold and thrust belt. Crustal structure beneath the KRBR station, located in the Central Iran domain consists of ~7-km thick sedimentary layer over ~40-km thick crystalline crust. Crust beneath SNGE, the only station located in Sanandaj–Sirjan zone consist of ~9-km thick sedimentary cover and a very thick crystalline crust with a thickness of ~50 km. Below SNGE, for some of the stacked RFs, an interface is observed at ~45-km depth.

4 Discussion

We determined the crustal velocity structure beneath the seven broadband seismic stations of INSN located in the Zagros, SSZ, UDMA, and the Central Iran by simultaneously inverting receiver functions and fundamental mode Rayleigh wave group and phase velocity measurements.

BNDS, GHIR, and SHGR are located in the Zagros fold and thrust belt. Our results indicate that the average crustal thickness beneath the Zagros Mountain

Fig. 8 Results of joint inversion of receiver function and fundamental-mode Rayleigh wave group velocity dispersion for stations SHGR, BNDS, SNGE, NASN, ASAO and KRBR for one of the back-azimuth bin receiver function stacks. For each station, the receiver function is at the upper right, the surface wave group velocity dispersion at the lower right, and the model at the left. *Black arrow* indicates inferred Moho. Other elements of the figure is the same as Fig. 5 ▶

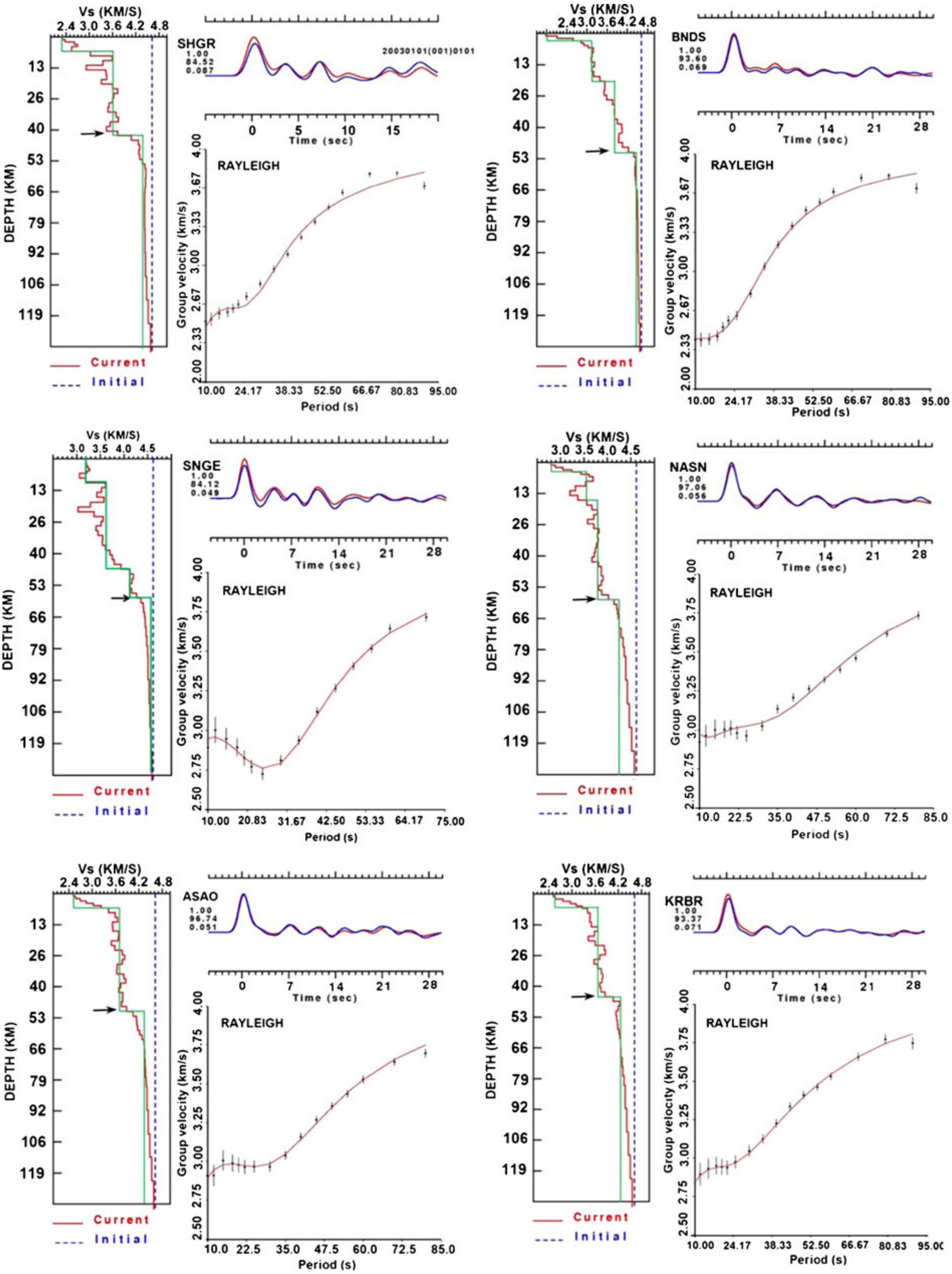
Vs (KM/S)
DEPTH (KM)
Current
Initial
SHGR
1.00
84.52
0.087
20030101(001)0101
Time (sec)
RAYLEIGH
Group velocity (km/s)
Period (s)
BNDS
1.00
93.60
0.069
SNGE
1.00
84.12
0.049
NASN
1.00
97.06
0.056
ASAO
1.00
96.74
0.051
KRBR
1.00
93.37
0.071

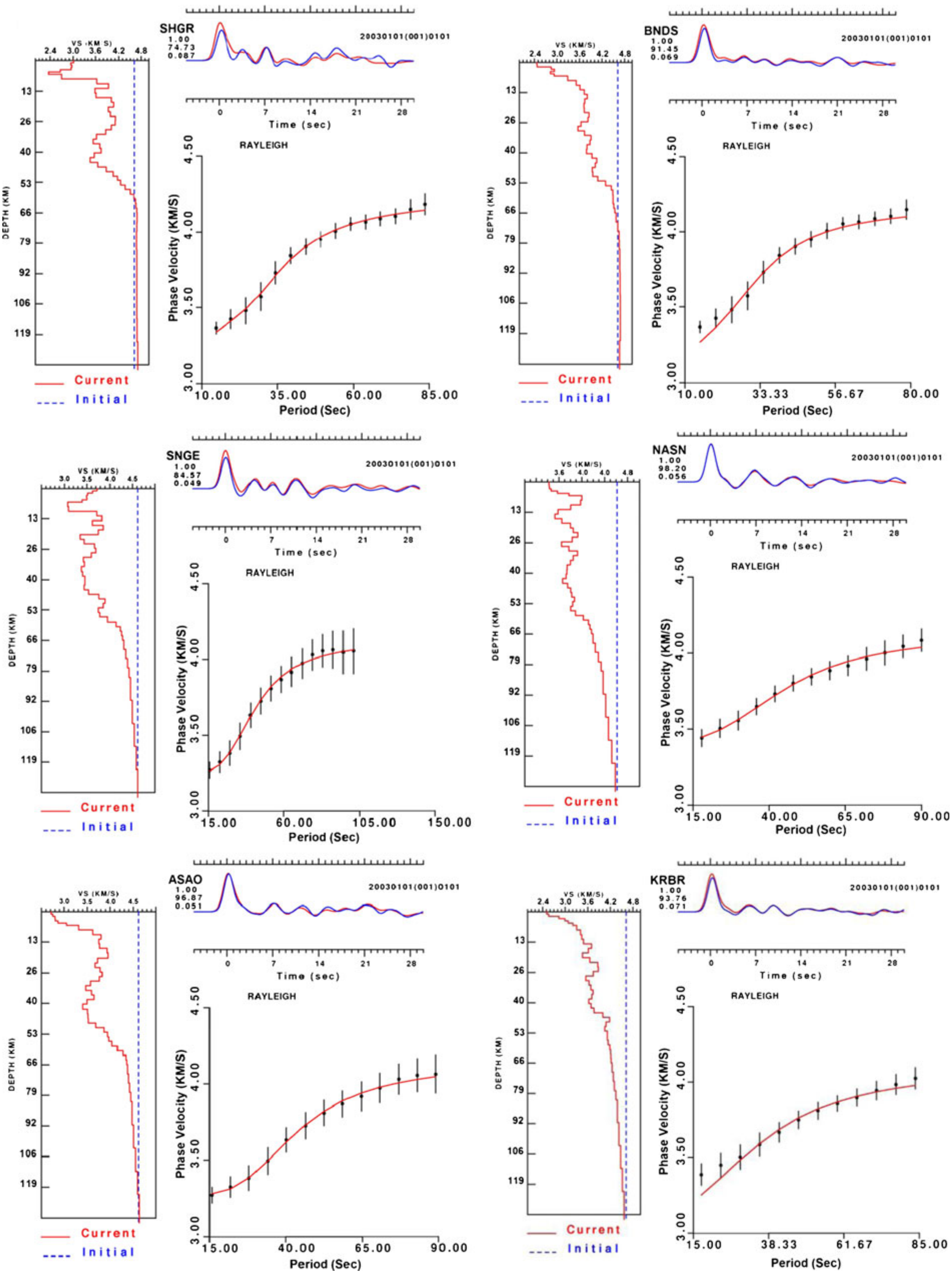
SHGR
1.00
74.73
0.087
20030101(001)0101
Time (sec)
RAYLEIGH
Phase Velocity (KM/S)
Period (Sec)
VS (KM/S)
DEPTH (KM)
Current
Initial
BNDS
1.00
91.45
0.069
20030101(001)0101
SNGE
1.00
84.57
0.049
20030101(001)0101
NASN
1.00
98.20
0.056
20030101(001)0101
ASAO
1.00
96.87
0.051
20030101(001)0101
KRBR
1.00
93.76
0.071
20030101(001)0101

◀ **Fig. 9** Results of joint inversion of receiver function and surface wave phase velocity dispersion for stations SHGR, BNDS, SNGE, NASN, ASAO, and KRBR for one of the back azimuth bin receiver function stacks. Rayleigh wave phase velocities computed for the closest path to the station which crosses the same structural units. Other elements of the figure is the same as Fig. 5

Range varies from ~46 km in Western and Central Zagros beneath SHGR and GHIR up to ~50 km beneath BNDS, located in easternmost of the Zagros. We found the same crystalline crust of ~34-km thick beneath the different parts of the Zagros fold and thrust belt, identical with total thickness of the crystalline crust (~35 km) proposed by Hatzfeld et al. (2003). Very gentle increase in the thickness of the sedimentary layer from western to eastern parts of the Zagros is the main reason for little observed variation in the Moho depth.

Toward SSZ and UDMA located NE of the Zagros, we observe an increase in Moho depth, where it reaches from ~46 km beneath the Central Zagros (GHIR) to ~58 km beneath SSZ (SNGE). Our results also reveal that the average thickness of the sedimentary cover varies from ~10–14 km in the Zagros fold and thrust belt to an average of ~6 km beneath SSZ, UDMA, and Central Iran. In spite of this observation, the crystalline crust is thickened beneath SSZ and UDMA considerably. In general, a crustal thickening is observed from the Arabian platform towards the main Zagros thrust fault and SSZ, as proposed by Snyder and Barazangi (1986) based on gravity data and Paul et al. (2006, 2010) based on seismological constrains. The thickening of the crust beneath the SSZ is related to overthrusting of the crust of the Arabian margin by the crust of Central Iran along the MZT (Paul et al. 2006).

Results of the joint inversion of receiver function and surface wave group and phase velocity dispersion below KRBR are consistent with a crystalline crust of ~40-km thick and a Moho located at ~47-km depth. A sedimentary layer, 7-km thick, obtained below KRBR is in good agreement with ~8 km of sedimentary cover reported by Tatar et al. (2005) for the Bam region located in the same tectonic zone. Most of the crustal structure studies show a moderate thickness for crust in Central Iran, (e.g., Giese et al. 1983; Dehghani and Makris 1984; Paul et al. 2006; Afsari et al. 2011).

Our observations indicate an increase of the average crustal thickness beneath the UDMA from ~50 km in western parts below ASAO to ~58 in central parts below NASN. The same thickening of the crust is observed beneath the SSZ from the northwestern to the central parts (Paul et al. 2010). The Moho depth is comprised between 69±2 and 56±2 km in central and northwest of SSZ, respectively (Paul et al. 2010).

5 Conclusion

The simple crustal velocity models have been derived through the joint inversion of stacked RFs and Rayleigh wave dispersion for seven permanent seismological stations located in the Zagros continental collision zone. Simplified models by amalgamating the thin layer with the same velocity as thicker layer show that all receiver functions can be well fitted using a three- or four-layer model, containing a sedimentary layer, and/or a mid-crustal discontinuity separating upper and lower crystalline crust, over the uppermost mantle. The error analysis showed that the estimated Moho depth could be offset up to ±2 km.

Our results show that the Moho under the stations is a sharp discontinuity that varies from ~46 km in Western and Central Zagros beneath SHGR and GHIR up to ~50 km beneath BNDS located in easternmost of the Zagros. However, the same crystalline crust of ~34-km thick was found beneath the different parts of the Zagros fold and thrust belt. The Moho depth reaches ~58 km beneath SNGE, indicating a considerable increase of crustal thickness from the Central Zagros toward the Sanandaj–Sirjan zone. An increase of the average crustal thickness is also observed beneath the UDMA from ~50 km in western parts below ASAO to ~58 in central parts below NASN. The Moho discontinuity beneath the KRBR station is located at ~47-km depth, revealing a moderate thickness of crust for Central Iran.

The observed variation along the SSZ and UDMA may be associated to ongoing slab steepening or break off in the NW Zagros, comparing underthrusting of the Arabian plate beneath Central Zagros as suggested by Mouthereau et al. (2012). However, the similarity of crustal structure below SHGR, GHIR, and BNDS suggests that the crust of the Zagros fold and thrust belt was uniform before subsidence and deposition of the sediments. Our results confirm that the shortening of the western and eastern parts of the Zagros basement is small and has only started recently as already suggested by Hatzfeld et al. (2003) for the Central Zagros.

Acknowledgments We would like to thank the Iranian National Seismic Network (INSN) for kindly providing the teleseismic recordings of their broadband stations. This research is supported by the International Institute of Earthquake Engineering and Seismology (IIEES) under research project 5327 entitled "Lithosphere structure of Iranian plateau using receiver functions and surface waves analysis". The authors would like to thank the anonymous reviewers for their helpful suggestions and comments. We used the computer programs in seismology (Herrmann and Ammon 2003) for data processing and GMT(Wessel and Smith, 1995) for plotting.

References

Abbassi A, Nasrabadi A, Tatar M, Yamini-Fard F, Abbassi MR, Hatzfeld D, Priestley K (2010) Crustal velocity structure in the southern edge of the Central Alborz (Iran). J Geodyn 49:68–78

Afsari N, Sodoudi F, TaghizadehFarahmand F, Ghassemi MR (2011) Crustal structure of Northwest Zagros (Kermanshah) and Central Iran (Yazd and Isfahan) using teleseismic Ps converted phases. J Seismol 15(2):341–353

Agard P, Omrani J, Jolivet L, Mouthereau F (2005) Convergence history across Zagros (Iran): constraints from collisional and earlier deformation. Int J Earth Sci. doi:10.1007/s00531-005-0481-4

Agard P, Omrani J, Jolivet L, Whitechurch H, Vrielynck B, Spakman W, Monié P, Meyer B, Wortel R (2011) Zagros orogeny: a subduction-dominated process. In: Lacombe O, Grasemann B, Simpson G (eds) Geodynamic Evolution of the Zagros. Geol Mag 692–725

Aki K, Richard PG (2002) Quantitative Seismology. Freeman, San Francisco

Alavi M (1994) Tectonics of the Zagros orogenic belt of Iran: new data and interpretations. Tectonophysics 229:211–238

Alavi M (2004) Regional stratigraphy of the Zagros fold-thrust belt of Iran and its proforeland evolution. Am J Sci 304:1–20

Allen M., Jackson JA, Walker R., 2004. Late Cenozoic reorganization of the Arabia–Eurasia collision and the comparison of short-term and long-term deformation rates. Tectonics 23. doi:10.1029/2003TC001530.

Ammon GJ (1991) The isolation of receiver effects from teleseismic P waveforms. Bull Seismol Soc Am 81:2504–2510

Ammon CJ, Randall GE, Zandt G (1990) On the non-uniqueness of receiver function inversions. J Geophys Res 95:15303–15318

Berberian F, Berberian M (1981) Tectonoplutonic episodes in Iran. In: Gupta HK, Delany FM (eds) Zagros–Hindu Kush–Himalaya Geodynamic Evolution. American Geophysical Union, Washington, pp 5–32

Berberian M, King GCP (1981) Towards a paleogeography and tectonic evolution of Iran. Can J Earth Sci 18

Berberian F, Muir ID, Pankhurst RJ, Berberian M (1982) Late Cretaceous and early Miocene Andean-type plutonic activity in Northern Makran and Central Iran. J Geol Soc Lond 139:605–614

Bird P (1978) Finite element modeling of lithosphere deformation: the Zagros collision orogeny. Tectonophysics 50:307–336

Bird P, Toksoz MN, Sleep NH (1975) Thermal and mechanical models of continent–continent convergence zones. J Geophys Res 32:4405–4416

Chang SJ, van der Lee S, Flanagan MP, Bedle H, Marone F, Matzel EM, Pasyanos ME, Rodgers AJ, Romanowicz B, Schmid C (2010) Joint inversion for three-dimensional S velocity mantle structure along the Tethyan margin. J Geophys Res 115, B08309. doi:10.1029/2009jb007204

Davoudzadeh M, Lammerer B, Weber-Diefenbach K (1997) Paleogeography, stratigraphy, and tectonics of the tertiary of Iran, Neues Jahrb. Geol Palaeontol Abh 205:33–67

Dehghani GA, Makris J (1984) The gravity field and crustal structure of Iran. N Jb Geol Palaontol Agh 168:215–229

Engdahl ER, Jackson JA, Myers SC, Bergman EA, Priestley K (2006) Relocation and assessment of seismicity in the Iran region. Geophys J Int 167:761–778

Giese P, Makris J, Akashe B, Rower P, Letz H, Mostaanpour M (1983) Seismic crustal studies in southern Iran between the Central Iran and Zagros belt. Geol Surv Iran 51:71–89

Golonka J (2004) Plate tectonic evolution of the southern margin of Eurasia in the Mesozoic and Cenozoic. Tectonophysics 381:235–273

Hatzfeld D, Tatar M, Priestley K, Ghafory-Ashtiany M (2003) Seismological constraints on the crustal structure beneath the Zagros Mountain belt (Iran). Geophys J Int 155:403–410

Hatzfeld D, Authemayou C, van der Beek P, Bellier O, LAVE' J, Oveisi B, Tatar M, Tavakoli F, Walpersdorf A, Yamini-Fard F (2010) The kinematics of the Zagros Mountains (Iran). Geol Soc Lond Spec Publ 330:19–42

Herrin E, Goforth T (1977) Phase-matched filters: application to the study of Rayleigh waves. Bull Seismol Soc Am 67:1259–1275

Herrmann RB, Ammon CJ (2003) Computer programs in seismology, Version 3.20, Surface waves, Receiver functions and Crustal structure, Saint Louis University, Penn State University

Jackson JA (1980) Reactivation of basement faults and crustal shortening in orogenic belts. Nature 283:343–346

Jackson J, McKenzie D (1984) Active tectonics of the Alpine–Himalayan Belt between western Turkey and Pakistan. Geophys J Roy Astron Soc 77:185–264

Julia J, Ammon CJ, Herrmann RB, Correig AM (2000) Joint inversion of receiver function and surface-wave dispersion observations. Geophys J Int 143:99–112

Langston CA (1979) Structure under Mount Rainier, Washington. The inferred from teleseismic body waves. J Geophys Res 84:4749–4762

Levshin AL, Ratnikova L, Berger J (1992) Peculiarities of surface-wave propagation across Central Eurasia. Bull Seismol Soc Am 82:2464–2493

Ligorria JP, Ammon CJ (1999) Iterative deconvolution and receiver function estimation. Bull Seismol Soc Am 89:1395–1400

Maggi A, Jackson JA, Priestley K, Baker C (2000) A reassessment of focal depth distributions in southern Iran, the Tien Shan, and northern India: Do earthquakes really occur in the continental mantle? Geophys J Int 143:629–661

Moghadam HS, Stern RJ, Rahgoshay M (2010) The Dehshir ophiolite (central Iran): geochemical constraints on the origin and evolution of the Inner Zagros ophiolite belt. Geol Soc Am Bull 122(9–10):1516–1547. doi:10.1130/ b30066.1

Molinaro M, Zeyen H, Laurencin X (2005) Lithospheric structure beneath the south-eastern Zagros Mountains, Iran: recent slab break-off? Terra Nova 17:1–6

Mouthereau F, Lacombe O, Vergés J (2012) Building the Zagros collisional orogen: timing, strain distribution, and the dynamics of Arabia/Eurasia plate convergence. Tectonophysics 532–535:27–60

Ni J, Barazangi M (1986) Seismotectonics of the Zagros continental collision zone and a comparison with the Himilayas. J Geophys Res 91(B8):8205–8218

Ozalaybey S, Savage MK, Sheehan AF, Louie JN, Brune JN (1997) Shear-wave velocity structure in the northern basin and range province from the combined analysis of receiver functions and surface waves. Bull Seismol Soc Am 87:183–199

Paul A, Kaviani A, Hatzfeld D, Vergne J, Mokhtari M (2006) Seismological evidence for crustal-scale thrusting in the Zagros mountain belt (Iran). Geophys J Int 166:227–237

Paul A, Kaviani A, Hatzfeld D, Tatar M, Priestley K (2010) Seismic imaging of thelithospheric structure of the Zagros Mountain belt (Iran). J Geol Soc Lond Spec Publ 330:5–18

Pedersen HA, Coutant O, Deschamps A, Soulage M, Cotte N (2003) Measuring surface wave phase velocities beneath smallbroad-band arrays: tests of an improved algorithmand application to the French Alps. Geophys J Int 154:903–912

Rapine R, Tilmann F, West M, Ni J (2003) Crustal structure of Northern and Southern Tibet from surface wave dispersion analysis. J Geophys Res 108:doi: 10.1029/2001JB000445

Rham D (2009) The crustal structure of the Middle East.Ph.D. thesis, University of Cambridge Library, Cambridge, UK

Shapiro NM, Singh SK (1999) A systematic error in estimating surface wave group-velocity dispersion curves and a procedure for its correction. Bull Seismol Soc Am 89:1138–1142

Simmons NA, Myers SC, Johannesson G (2011) Global-scale P wave tomography optimized for prediction of teleseismic and regional travel times for Middle East events: 2. Tomographic inversion. J Geophys Res 116: (B04305). doi:10.1029/2010jb007969

Snyder DB, Barazangi M (1986) Deep crustal structure and flexure of the Arabian Plate beneath the Zagros collisional mountain belt as inferred from gravity observations. Tectonics 5:361–373

Stocklin J (1968) Structural history and tectonics of Iran: a review. Am Assoc Petrol Geol Bull 52:1229–1258

Stöcklin J (1974) Possible ancient continental margins in Iran. In: Burke C and Drake C (eds) Geology of Continental Margins. New York, 873–877

Stoneley R (1981) The geology of the Kuh-e Dalneshin area of Southern Iran, and its bearing on the evolution of Southern Tethys. J Geol Soc Lond 138:509–526

Tatar M, Hatzfeld D, Ghafory-Ashtiany M (2004) Tectonics of the Central Zagros (Iran) deduced from microearthquakes seismicity. Geophys J Int 156:255–266

Tatar M, Hatzfeld D, Moradi AS, Paul A (2005) The 2003 December 26 Bam earthquake (Iran), Mw 6.6, aftershock sequence. Geophys J Int 163:90–105

Tezel T, Erduran M, Alptekin O (2007) Crustal shear wave velocity structure of Turkey by surface wave dispersion analysis. Ann Geophys 50:177–190

Vergés J, Goodarzi MH, Emami H, Karpuz R, Efstatiou J, Gillespie P (2011) Multiple detachment folding in Pusht-e Kuh Arc, Zagros. Role of mechanical stratigraphy. In: McClay, K., Shaw, J., Suppe, J. (eds) Thrust Fault Related Folding: AAPG Memoir, 94: 69–94. Chapter 4

Vernant P, Nilforoushan F, Hatzfeld D, Abbassi M, Vigny C, Masson F, Nankali H, Martinod J, Ashtiani A, Bayer R, Tavakoli F, Chery J (2004) Present-day crustal deformation and plate kinematics in the Middle East constrained by GPS measurements in Iran and northern Oman. Geophys J Int 157:381–398

Walker RT, Andalibi MJ, Gheitanchi MR, Jackson JA, Karegar S, Priestley K (2005) Seismological and field observations from the 1990 November 6 Furg (Hormozgan) earthquake: a rare case of surface rupture in the Zagros Mountains of Iran. Geophys J Int 163:567–579. doi:10.1111/ j.1365-246X.2005.02731.x

Walpersdorf A et al (2006) Difference in the GPS deformation pattern of North and Central Zagros (Iran). Geophys J Int 167:1077–1088. doi:10.1111/j.1365-246X.2006.03147.x

Wessel P, Smith W (1995) New version of the Generic Mapping Tool release. Eos Trans AGU 76:329

Wiener N (1949) Extrapolation, Interpolation, and Smoothing of Stationary Time Series. Wiley, New York

Yamini-Fard F, Hatzfeld D, Tatar M, Mokhtari M (2006) Microearthquake seismicity at the intersection between the Kazerun fault and the Main Recent Fault (Zagros, Iran). Geophys J Int 166:186–196. doi:10.1111/j.1365-246X.2006.02891.x